This is a preprint, the final version is subject to change, of the American Mineralogist (MSA)
Cite as Authors (Year) Title. American Mineralogist, in press.
DOI: http://dx.doi.org/10.2138/am-2018-6242

Revision 2.

Submicronic yttrian zircon coating and arborescent aeschynite microcrystals on truncated bipyramidal anatase: An electron microscopy study of miarolitic cavities in the Cuasso al Monte granophyre (Varese, Italy).

Giancarlo Capitani[1]*, Enrico Mugnaioli[2] and Paolo Gentile[1]

[1] Department of Earth and Environmental Sciences, University of Milano-Bicocca, Piazza della Scienza 4, Milan 20126 (Italy)

[2] Center for Nanotechnology Innovation@NEST, Istituto Italiano di Tecnologia, Piazza San Silvestro 12, Pisa 56127 (Italy).

*corresponding author: giancarlo.capitani@unimib.it

Abstract

In this paper, we describe a unique occurrence of submicronic polycrystalline zircon and arborescent aeschynite microcrystals on anatase with truncated bipyramidal habit, which were formed during low-temperature hydrothermal alteration of miarolitic cavities in a granophyre from Cuasso al Monte (Italy). The results suggest that temperatures in the range 100-250 °C and acidic conditions

characterized the formation of anatase and that the preservation of this metastable phase was due to the presence of Nb (Nb/Ti atomic ratio ~0.032). We also detected an increase in the Nb content along the anatase rim. This is related to the incipient segregation of Nb driven by the transition towards the thermodynamically more stable rutile phase, which is possibly arrested by cooling below the diffusion blocking temperature. In these samples, zircon clearly postdates anatase and predates aeschynite. The resulting possible scenario is that F-rich hydrothermal fluids altered primary minerals at relatively high temperature and then, on cooling below 250 °C, deposited, in the following sequence, anatase, zircon, and aeschynite, which reflects both elemental saturation and the fluid fractionation with decreasing temperature. Finally, the aeschynite identified in this study through TEM-EDS shows an unusual chemical composition $[(Fe_{0.35}Ca_{0.22}Th_{0.15}U_{0.13}Y_{0.10}Pb_{0.11})_{\Sigma=1.06}(Nb_{1.05}Ti_{0.69}Al_{0.14}As_{0.06})_{\Sigma=1.94}O_6]$, which cannot be reconciled with any known aeschynite sub-species. Conventional classification suggests that it should be called niobioaeschynite-(Y), although Y is present at only 0.10 a.p.f.u., and Fe (0.35 a.p.f.u.) predominates in the A-site. This suggest that the aeschynite-group mineral classification system should be re-considered.

Key-words: anatase, zircon, aeschynite, transmission electron microscopy (TEM), electron diffraction tomography (EDT).

Introduction

Anatase is one of the three natural polymorphs of TiO_2, the other two being rutile and brookite. Minimum-energy structural configuration energies calculated using the electron-gas model (Post and Burnham 1986) show that the rutile is more stable with respect to anatase and brookite by 4.0 kJ/mole, and 20 kJ/mole, respectively. Rutile is the stable polymorph as bulk crystal at all temperatures and

pressures (Smith et al. 2009) and, not surprisingly, the recurrent TiO_2 phase in nature. Notwithstanding, anatase tends to form metastably under low-temperature hydrothermal conditions. Moreover, anatase is stable with respect to rutile when the TiO_2 particle size is in the nanometer range (Zhang and Banfield 1998; Barnard and Curtiss 2005) because of its lower surface energy (0.74 vs. 2.22 J/m^2, respectively; Levchenko et al. 2006). Anatase is tetragonal (space group = $I4_1/amd$, a = 3.784, c = 9.515 Å; Horn et al. 1972) with a structure based on CCP anions and consists of TiO_6 octahedra that share four edges with other such octahedra (Fig. 1a).

Zircon ($ZrSiO_4$) is a common accessory mineral occurring in a wide variety of igneous, metamorphic, and sedimentary rocks, in the latter case as detrital rather than as authigenic mineral. Reports on hydrothermal zircon are rare and mostly refer to low-temperature and low-pressure events associated with ore mineral deposition (Hoskin and Schaltegger 2003). The ability to incorporate minor and trace elements makes zircon a source of isotopic information and a desirable candidate for geochemical studies, including the ones concerning the evolution of the Earth's crust and mantle, as well as geochronological applications. Able to resist to several geological cycles, zircon is a major constituent in the heavy-mineral fractionation of sediments and is widely used in rock source provenance studies (Harley and Kelly 2007). Because of its chemical and physical durability, zircon has been proposed as candidate waste form for the long-term geological disposal of actinides from dismantled nuclear weapons and spent nuclear fuel (Ewing et al. 1999). The large number of applications makes zircon one of the most studied minerals.

Zircon crystallizes in the same space group $I4_1/amd$, as anatase, with cell parameters a = 6.604, c = 5.979 Å (Robinson et al. 1971). The structure consists of ZrO_8 dodecahedra that share edges with each other and form chains parallel the two equivalent [100] and [010] directions. The chains are cross-

linked by isolated, corner sharing SiO_4 tetrahedra. The Si and Zr polyhedral also form edge-sharing chains of alternating SiO_4 and ZrO_8 polyhedra along [001] (Fig. 1b).

Aeschynite is a typical accessory mineral in granitic pegmatites (Černy and Ercit 1989), where it usually precipitates during the late-stage magmatic phase from Nb-, Ti-, Y-, HREE-enriched and F-depleted fluids (Hanson et al. 1992). It has also been reported as a secondary mineral in hydrothermal alteration of Ti-silicates such as titanite (Papoutsa and Pe-Piper 2013, Pro-Ledesma et al. 2012), and chevkinite (MacDonald et al. 2015). Aeschynite has the general formula AB_2O_6, where A is 8-fold coordinated in a typical square antiprism and mostly occupied by Y, REE, Ca, and U, and B is 6-fold coordinated and mostly occupied by Ti, Nb, and Ta. The structure is orthorhombic with space group *Pnma* and cell parameters a = 10.803-11.031, b = 7.448-7.532, and c = 5.150-5.189 (Bonazzi and Menchetti 1999). It consists of pairs of edge-sharing BO_6 octahedra connected by corners to form double chains running in a zigzag pattern along the [010] (Aleksandrov 1962).

In this study, we, employ scanning (SEM) and transmission electron microscopy (TEM), precession-assisted electron diffraction tomography (P-EDT), and energy dispersive spectroscopy (EDS) to describe a unique occurrence of submicroscopic polycrystalline zircon and arborescent aeschynite microcrystals on anatase with a truncated bipyramidal habit, which were formed during low-temperature hydrothermal alteration of miarolitic cavities in a granophyre from Cuasso al Monte (Italy). With this study, we aim to contribute to the understanding of remobilization and fractionation of incompatible rare-earth elements (REE, including Y), actinides (U, Th), and high-field strength elements (HFSE) such as Zr, Nb and Ti, during post-magmatic hydrothermal stages. This is fundamental in order to determine the complete history of the host rocks and, as a consequence, the mineralizing potential of the fluids and the value of the U/Pb and Th/Pb absolute dating.

Sample and Geological outlines

Anatase crystals with a zircon coating were found in millimeter sized miarolitic cavities in a granophyre from Cuasso al Monte. The Cuasso al Monte granophyre is a sialic hypoabyssal rock composed essentially of K-feldspar, albite, quartz, and minor biotite. Known by the commercial name of *Red Porphyry*, it is greatly appreciated for its warm and vivid color, hardness and resistance to erosion, and for these reasons largely employed to create floorings, coverings, and building elements.

The red porphyry crops out uninterruptedly along the western shore of Lake Lugano until Monte Martica (Fig. 2), and is genetically associated with a late Hercynian post-orogenic magmatism of K-rich alkaline affinity from intermediate to acidic composition, known as the "Serie dei Laghi" (Boriani et al. 1992). The magma was emplaced either as andesitic to rhyolitic ignimbrites or as pink subsolvus granites at subvolcanic levels (Bakos et al. 1990). Isotopic investigations showed that it was generated from a mantle-derived primary magma that experienced crustal contamination (Pinarelli et al. 1993, 2002). The most felsic products (including the red porphyry) appear to have been generated mainly by crystal fractionation processes from an intermediate magma, already contaminated.

The representative bulk composition of the red porphyry is 75.26% SiO_2, 13.39% Al_2O_3, 5.11% K_2O, 3.37% Na_2O, 1.14% FeO, 0.85% H_2O, 0.75% CaO, 0.25% Fe_2O_3, 0.10% MgO, 0.09% P_2O_5, 0.08 TiO_2, and 0.03% MnO. Rb/Sr dating indicates an age of 275±8 Ma (Bakos et al. 1990). Millimeter sized miarolitic cavities are widespread within the granophyre. Circulation of abundant late hydrothermal fluids was responsible for the local alteration of feldspars, chloritization of biotite, and the deposition of abundant carbonates, fluorite, and sulfides in the miarolitic cavities (Pezzotta et al. 1999, 2005). In the present study, in addition to K-feldspar, albite, and quartz, we found chamosite, fluorite, REE-carbonates, sphalerite, anatase (with zircon coating), and aeschynite (Fig. 3), the latter determined by TEM.

Experimental Methods

SEM-EDS investigations on carbon-coated sample fragments were performed at the Department of Earth and Environmental Sciences at the University of Milano-Bicocca with a Tescan VEGA TS 5136XM instrument operating at 20 keV and equipped with an EDAX GENESIS 4000XMS EDS system.

TEM observations were performed at the Department of Physical Sciences, Earth and Environment of the University of Siena with a JEOL JEM 2010 operating at 200 keV. Images were collected on Fuji imaging plates (3000 × 3760 pixels × 14 bit) and with an Olympus Tengra CCD camera (2k × 2k pixels × 14 bit). TEM foils were prepared using the FIB technique (Wirth 2009) at the German Research Center for Geosciences (GeoForschungsZentrum GFZ), Postdam, Germany). In addition, micron-size aeschynite crystals were picked up using a micromanipulator and deposited on carbon-coated Cu-grids.

TEM energy dispersive X-rays analyses were collected using two different systems: An Oxford Link EDS spectrometer attached to the JEOL JEM 2010 of Siena University; and an EDAX EDS spectrometer attached to a FEI Tecnai 20F (Department of Earth Sciences, Milano University). In both cases, the standardless method within the Cliff-Lorimer approximation (Cliff and Lorimer 1975) were used for semi-quantitative analyses.

Precession-assisted electron diffraction tomography (P-EDT) was performed operating the JEOL JEM 2010 (Siena University) in selected area electron diffraction (SAED) mode and in combination with a SpinningStar precession device (NanoMEGAS). SAED patterns were acquired with the Olympus Tengra CDD camera. Two acquisition series were performed. One rotated the sample around the α-axis and the other rotated the sample around the β-axis of the specimen holder. For cell

parameter determination, only the α-tilt acquisition was used. For *ab-initio* structure determination and refinement, intensities from both acquisitions were merged with scale factor 1. Structure solution was obtained *ab-initio* by direct methods as implemented in the SIR2014 program (Burla et al. 2015) employing reflections up to 0.8 Å resolution and adopting a fully kinematical approximation ($I_{hkl} \sim F_{hkl}^2$). Structure refinement was performed with the least-square method as implemented in the SHELX-97 program (Sheldrick 1997). Since electron scattering factors for Th, Y, and Nb are currently not available (Doyle & Turner 1968), U, Zr, and Mo scattering factors were used, respectively.

Results

The anatase crystals are ~50 microns in size and show a truncated bipyramidal habit, with ragged surfaces (Fig. 4a). Some growth features, possibly etch marks, are also observed on pinacoidal and pyramidal faces. In certain areas, arborescent crystals are also present (Fig. 4b). These crystals were identified as aeschynite-group minerals by subsequent TEM investigations (see below). High magnification observations using SEM reveal that the ragged appearance of the anatase is due to submicronic lenticular crystals in random orientations (Fig. 4c), whose major elements are Ti, Zr, Si, and O from SEM-EDS spectra, suggesting a mixture of anatase and zircon. Bright field TEM images and SAED patterns on FIB foils incorporating these crystals, confirm that a thin 0.3 micron thick layer of zircon crystals surrounds the anatase. The zircon crystals have a lenticular shape, a few hundreds of nanometers long, which are inclined relative to the anatase surface (Fig. 4d). The zircon crystals appear to have nucleated on the periphery of anatase, from which they are separated by a band about one hundred nanometers thick, characterized by a strong strain contrast. The dimension of the zircon crystals and their average separation are of the order of the wavelength of visible light, i.e. few

158 hundreds of nanometers. This observation may explain why the anatase crystals appear iridescent at the
159 optical stereomicroscope (s. Fig. 3b).

160 TEM-EDS spot analyses were taken on anatase, zircon, and on the interface between the two
161 with a nominal spot size of 25 nm. Average compositions of anatase and zircon are reported in Table 1.
162 Up to 0.32 atoms per formula unit of Y were detected in zircon and detectable amount of Nb in both
163 zircon and anatase. A compositional profile from anatase to zircon along a distance of about 600 nm
164 across the interface is reported in the graph in Figure 5. It should be noted how the Nb concentration
165 forms a maximum along the anatase rim, close to zircon. A possible explanation could be that the
166 highly defective local structure at the zircon-anatase interface, as implied by the strong strain contrast,
167 could provide a better coordination environment for Nb than in the adjoining ordered phases.
168 Alternatively, this feature may indicate a diffusion of Nb from anatase towards the rim, revealing an
169 incipient anatase-to-rutile phase transition (see discussion section).

170 Some arborescent crystals were picked up with a micromanipulator, deposited on carbon-coated
171 Cu-grids and examined by TEM. A representative crystal is shown in Figure 6, along with the related
172 SAED pattern and EDS spectrum. P-EDT allowed an *ab-initio* structure determination, which was fully
173 consistent with the aeschynite-group mineral structure (Fig. 1c; cf. Table 2 for the relevant
174 experimental and crystallographic data[1]). Crystals are blade shaped, elongated along [010], and
175 flattened on (001). Surprisingly, EDS spectra taken with three different spectrometers, either on TEM
176 or SEM, revealed a peak at 1.74 KeV that was systematically labeled as $Si_{K\alpha}$ by the automatic peak
177 assignment routine of the EDS system. However, it is well known that Si, which is always in
178 tetrahedral coordination at ambient conditions, cannot be hosted in the aeschynite structure, which
179 contains only octahedral or larger cation sites. Since the $Ta_{M\alpha1}$ line at 1.71 KeV falls close to the $Si_{K\alpha1}$

[1] The crystallographic information file (CIF) provided as supplementary material

line and cannot be easily discriminated with EDS systems, Ta, which is a common constituent of aeschynite-group minerals, was assumed to be part of the composition. However, no reasonable peak fitting, nor a consistent chemical formula were obtained with Ta, which was often rejected by the quantification routine, pointing to the absence of $TaL_{\alpha 1}$ at 8.15 keV and $TaL_{\beta 1}$ at 9.34 keV in the spectra. Silicon was thus suspected to be present as silica inclusions or within metamict areas of the sample. This is supported by the bright field (BF) images of the aeschynite, which show a mottled contrast typical of metamict minerals (Fig. 6a) and high resolution (HR) images, which show brighter domains lacking lattice fringes indicative of long range order (Fig. 6c). Although no compositional differences between the dark and bright domains could be spotted because the size of the domains is smaller than the actual TEM-EDS probe, the domains were assumed to contain Si, as often observed in other metamict minerals (e.g., Bonazzi et al. 2006, 2009). Silicon was therefore not considered in the derivation of the chemical formulae of aeschynite, which are reported in Table 3 for the three crystals investigated in this study. It should be noted that their composition varies considerably from crystal to crystal and within the same crystal, especially with regard to the Ti/Nb ratio. Moreover, all crystals contain large amount of Fe that was assumed to be Fe^{2+} and assigned to the A-site in order to fit the aeschynite-group mineral stoichiometry. In one case (crystal 3), a significant excess of A-site cations and a deficiency of B-site cations arises, which may indicate that part of the Fe is oxidized and occupies the B-site. The average chemical composition of the investigated crystals calculated on the basis of 3 cations comes out as $(Fe_{0.35}Ca_{0.22}Th_{0.15}U_{0.13}Y_{0.10}Pb_{0.11})_{\Sigma=1.06}(Nb_{1.05}Ti_{0.69}Al_{0.14}As_{0.06})_{\Sigma=1.94}O_6$, which identifies the mineral as niobioaeschynite, but deviates considerably from any known aeschynite species considering the exceptionally high Fe content that predominates in the A-site.

Discussion and conclusions

Several authors have suggested a strong hydrothermal alteration for many rocks of the "Serie dei laghi" suite, including the granophyre from Cuasso al Monte (e.g., Bakos et al. 1990, Pinarelli et al. 1993, 2002, Pezzotta et al. 1999, 2005). As reported by Pezzotta et al. (2005), a massive liberation of fluids occurred because of the saturation levels attained during the crystallization of the silicic melt. These fluids produced an alteration that changed the color of K-feldspar to pink, transformed biotite to chlorite, and altered the Ca-rich plagioclase to late stage albite, epidote, and calcite.

A series of hydrothermal minerals were deposited in the miarolitic cavities with decreasing temperature during this stage. Pezzotta et al. (2005), in a study of Sc-silicates found in these miarolytic cavities, suggest two possible models to explain their mineral assemblage, one of which is consistent with a late hydrothermal alteration. According to this hypothesis, HFSE, Sc, and Y+REE were first incorporated into gadolinite-(Y) and siderophyllite crystallizing from the residual magma. The subsequent, aggressive effect of subcritical hydrous F-rich fluids on early formed gadolinite-(Y), siderophyllite, and feldspars provided the necessary elemental source (REE, Y, Fe, Ca, Ti, and possibly Nb, Ta, Sc, etc.) for the crystallization of secondary minerals. The anatase, zircon, aeschynite, and minor REE-carbonates from the miarolitic cavities, and described in this study, may have formed from F-rich fluids.

In nature, anatase is known to form under low-temperature hydrothermal conditions. For example, in epithermal Au systems the anatase-to-rutile transformation occurs at 150-200 °C (Hedenquist et al. 2000). Papoulis et al. (2009), in a study of volcanic rocks from the Limnos Island (Greece), report the formation of halloysite and anatase from hydrothermal alteration of ilmenite and biotite at temperatures as low as 100 °C. In a recent study, Andersen et al. (2016) describe an anatase-xenotime-brockite-fluorite mineral assemblage in carbonatite dikes and veins peripheral to the Bear Lodge alkaline complex (Wyoming), formed from low-temperature (<200 °C), F-rich fluids. Sabyrov

et al. (2012) hydrothermally processed anatase nanoparticles at 250 °C and a pH 1 and 3, obtaining the rutile phase. They also found that the anatase-to-rutile transition and rutile particle growth rates increase as the initial anatase particle size and pH decrease. These observations suggest that anatase at Cuasso al Monte may have formed in a temperature range of 100-250 °C.

Barnard and Curtiss (2005) investigated the effects of surface chemistry on the morphology and phase stability of TiO_2 nanoparticles using a thermodynamic model based on surface free energy obtained from first principle calculations. They found that anatase nanoparticles are stabilized with respect to rutile by surface adsorbates containing a large amount of hydrogen, i.e. in acidic conditions. Moreover, the crystal morphology is truncated bipyramidal under hydrogenated conditions, but starts to develop tetragonal prism facets under progressively lower hydrogenated conditions. This is in agreement with the fact that experimental synthesis of TiO_2 nanoparticles in acidic conditions almost exclusively result in truncated tetragonal anatase bipyramids with {101}, {001}, and {010} facets (Penn and Banfield 1999, Zaban et al. 2000, Gao and Elder 2000). These observations suggest that truncated bi-pyramidal anatase from Cuasso al Monte probably formed under acidic conditions. Bulk anatase, however, is metastable with respect to rutile at all temperatures and pressures (Smith et al. 2009), therefore, how could it remain stable during growth?

In annealing experiments between 600 and 900 °C, Arbiol et al. (2002) reported that the anatase-to-rutile phase transition is strongly hindered for Nb-doped TiO_2 samples. Before and during the phase transition, for amounts of Nb higher than 2-3% Nb/Ti atoms, they observed NbO segregation at the rims of the TiO_2 nanoparticles. Similarly, Hirano and Sato (2011), in annealing experiments between 800 and 1200 °C, found that the anatase-to-rutile transition in Y and Nb co-doped samples ($Y_{1-x}Nb_{1-x}Ti_{1-2x}O_2$, x = 0-0.20) is shifted towards higher temperatures. They also noticed a $YTiNbO_4$ aeschynite-type structure as a coexisting reaction product.

These high-temperature experiments suggest that Nb could be an inhibiting agent in the anatase-to-rutile transformation even at low temperature, since Nb can enter the TiO_2 structure through two principal heterovalent substitutions:

$$5Ti^{4+} \rightarrow 4Nb^{5+} + \square \quad (1)$$

$$2Ti^{4+} \rightarrow Nb^{5+} + Ti^{3+} \quad (2)$$

Both substitutions cause local charge unbalance and lattice strain because of the different charge and ionic radius of the involved octahedrally coordinated cations, namely Ti^{4+} (ionic radius = 0.61 Å), Nb^{5+} (0.64), and Ti^{3+} (0.67) (Shannon 1976). In addition, substitution (1) cause cation vacancies. Simple crystal chemistry considerations suggest that the anatase structure can tolerate higher cation vacancies, and therefore higher Nb content, than the rutile structure. In fact, Ti-octahedra share four edges in anatase and only two in rutile. It follows that local charge unbalance can be better compensated by neighboring Ti cations in anatase than in rutile. Experimental results confirm this hypothesis, since anatase and rutile prepared from the same solution and heat treated at 600 °C show 20% and 10% of cation vacancies, respectively (Bokhimi et al. 1995). On the other hand, the high value of the rutile bulk module (210 GPa) compared with that of anatase (178 GPa), suggests that the introduction of sterically costing defects in rutile would require a higher energy per defect than in the case of anatase (Arbiol et al. 2002 and references therein). In summary, temperatures in the range 100-250 °C and low pH conditions led to the formation of anatase at Cuasso al Monte. The preservation of the metastable phase may be due to the presence of Nb (Nb/Ti atomic ratio ~0.032). On the other hand, the increase of the Nb content along the anatase rims may indicate an incipient segregation of Nb driven by the transition towards the thermodynamically more stable rutile phase, possibly arrested by cooling below the diffusion blocking temperature.

Hydrothermal zircon typically forms at temperatures between 600 °C (magmatic-to-hydrothermal transition) and 300 °C (mesothermal ore-forming systems) (Schaltegger 2007). However, Bojanowsky et al. (2012) reported the formation of authigenic zircon in Mississippian shales (Scotland) at around 270°C. Rasmussen (2005) reported about minute (typically <3 μm) zircon outgrowths on detrital grains in low-grade sedimentary rocks from different regions of the world at ~250°C, and related their growth to the transport of Zr in aqueous fluids, possibly as F-complexes. Hay and Dempster (2009), in a study of detrital zircon in Carboniferous sandstones from Scotland, showed that metamict zircon alters and recrystallizes to nanocrystalline zircon at temperatures below 100 °C through a dissolution-reprecipitation process. This would imply that Zr can be remobilized at low temperatures and stabilized in the fluid in the presence of F until the combined effects of decreasing temperature and decreasing F-activity, possibly related to the crystallization of fluorite, cause the breakdown of Zr-complexes and the precipitation of low-temperature nanocrystalline zircon.

Recent experimental studies (i.e., Rapp et al. 2010, Tanis et al. 2015, Timofeev et al. 2015), although performed at *T* and *P* conditions beyond the range expected for Cuasso al Monte, demonstrate that the solubility and aqueous complexation of Ti^{4+} and Nb^{5+} is extremely high in F-rich solutions, and that the removal of F during precipitation of F-bearing minerals decreases Ti+Nb solubility and promotes the crystallization of (Ti+Nb)-bearing minerals.

In the granophyre at Cuasso al Monte, the zircon coating on the anatase crystals clearly postdates the anatase and predates the aeschynite. A possible scenario is that F-rich hydrothermal fluids altered the primary minerals at relatively high temperature and then, on cooling, deposited anatase, zircon and aeschynite in a sequence, which reflects elemental saturation and fluid fractionation with decreasing temperature over a range between 250 and 100 °C. At the same time, few REE-carbonates formed in pockets during this latest stage, testifying to the minor presence of CO_2 in the fluid.

Implications

In this study we describe a unique occurrence of microscopic anatase with a truncated bipyramidal habit coated with submicronic polycrystalline zircon and arborescent aeschynite microcrystals, deposited under low-pressure (< 500 bar; Bakos et al. 1990), low-temperature (250-100 °C), low pH, hydrothermal conditions. While anatase is known to form under these conditions, the genesis of zircon, associated with hydrothermal activity, is usually placed between 600 and 300 °C (Schaltegger 2007), though there are exceptions to this rule (e.g., Bojanowsky et al. 2012, Rasmussen 2005, Hay and Dempster 2009). In this work, we propose that Zr could be remobilized from primary minerals and recrystallized as new zircon at temperatures lower than 250 °C. This finding implies that secondary zircon might be used for the dating late-stage hydrothermal activities in magmatic rocks. On the other hand, it also suggests that the value of U/Pb and Th/Pb geochronological studies involving zircon could be affected by late-stage remobilization of Th and U from the primary accessory minerals, as testified by the significant amount of these actinides in the aeschynite-group minerals.

EDS analyses are generally considered semi-quantitative, but sufficiently accurate for mineral identification (e.g., Ramussen 2005, Papoutsa and Pe-Piper 2013, Capitani 2017), especially if a complementary technique is used for the characterization of the mineral, as in this case, i.e., electron diffraction tomography. The aeschynite identified in this study possess an unusual chemical composition that cannot be reconciled with any known member of the aeschynite supergroup. It should be named, according to the current nomenclature on rare earth minerals (Bayliss and Levinson 1988) niobioaeschynite-(Y), because Y, although present with only 0.10 a.p.f.u., is the only REE at the A-site, being Fe (0.35 a.p.f.u.) the predominant cation at this site, followed by Ca (0.22). The finding of this unusual aeschynite composition asks for a reconsideration of the classification of this mineral group.

317

318 **Acknowledgements**

319 Anja Schreiber and Richard Wirth (GFZ, Postdam, Germany) are greatly acknowledged for preparation
320 of TEM foils. Paola Bonazzi and Bernad Grobéty provided thoughtful revisions that greatly improved
321 the quality of the manuscript.

322

323 **References**

324 Aleksandrov, V.B. (1962) The crystal structure of aeschynite. Doklady Akademii Nauk SSSR, 142,
325 181-184. English translation in Doklady of the Academy of Sciences of the USSR. Earth Sciences
326 Sections, 142, 107–109.

327 Andersen, A.K., Clark, J.G., Larson, P.B., Neill, O.K. (2016) Mineral chemistry and petrogenesis of a
328 HFSE (+HREE) occurrence, peripheral to carbonatites of the Bear Lodge alkaline complex, Wyoming.
329 American Mineralogist, 101, 1604–1623.

330 Arbiol, J., Cerdà, J., Dezanneau, G., Cirera, A., Peiró, F., Cornet, A., Morante, J. R. J. (2002) Effects of
331 Nb doping on the TiO_2 anatase-to-rutile phase transition. Journal of Applied Physics, 92, 853–861.

332 Arroyo, R., Córdoba, G., Padilla, J., Lara, V.H. (2002) Influence of Manganese ions on the anatase-
333 rutile phase transition of TiO_2 prepared by the sol-gel process. Materials Letters, 54, 397–402.

334 Bakos, F., Del Moro, A., Visonà, D. (1990) The Hercynian volcano-plutonic association of Ganna
335 (Lake Lugano, Central Southern Alps, Italy). European Journal of Mineralogy, 2, 373–383.

336 Barnard, A.S. and Curtiss L.A. (2005) Prediction of TiO_2 nanoparticle phase and shape transitions
337 controlled by surface chemistry. Nano Letters, 5, 1261–1266.

Bayliss, P. and Levinson, A.A. (1988) A system of nomenclature for rare-earth mineral species: Revision and extension, American Mineralogist, 73, 422–423.

Bojanowski, M.J., Bagiński B., Clarkson, E., Macdonald, R., Marynowski, L. (2012) Low-temperature zircon growth related to hydrothermal alteration of siderite concretions in Mississippian shales, Scotland. Contribution to Mineralogy and Petrology, 164, 245–259.

Bonazzi, P., Bindi, L., Zoppi, M., Capitani, G.C., Olmi, F. (2006) Single-crystal diffraction and transmission electron microscopy studies of silicified pyrochlore from Narssârssuk, Julianehaab district, Greenland. American Mineralogist, 91, 794–801.

Bonazzi, P., Holtstam, D., Bindi, L., Nysten, P., Capitani, G.C. (2009) Multi-analytical approach to solve the puzzle of a mineral from Kesebol, Västra Götaland, Sweden, belonging to the allanite-subgroup. American Mineralogist, 94, 121–134.

Bonazzi, P. and Menchetti, S. (1999) Crystal chemistry of aeschynite-(Y) from the Western Alps: residual electron density on difference-Fourier map. Europena Journal of Mineralogy, 11, 1043–1049.

Boriani, A., Burlini, L., Caironi, V., Giobbi Origoni, E., Sassi, A., Sesana, E. (1988) Geological and petrological studies on the hercynian plutonism of Serie dei Laghi. Geological map of its occurrence between Valsesia and Lago Maggiore (N-Italy). Rendiconti della Società Italiana di Mineralogia e Petrografia, 43, 367–384.

Boriani, A., Caironi, V., Giobbi Origoni, E., Vannucci, R. (1992) The Permian intrusive rocks of Serie dei laghi (Western Southern Alps). Acta Vulcanologica, 2, 73–86.

Burla, M.C., Caliandro, R., Carrozzini, B., Cascarano, G.L., Cuocci, C., Giacovazzo, C., Mallamo, M., Mazzone, A. Polidori, G. (2015) Crystal structure determination and refinement via SIR2014. Journal of Applied Crystallography, 48, 306–309.

Capitani, G.C. (2017) Complex exsolution microstructures in ilmenite-pyrophanite from the Garnet Codera dike pegmatite (Central Italian Alps): An electron microscopy investigation. Mineralogical Magazine, in press.

Capitani, G.C., Mugnaioli E, Guastoni, A. (2016) What is the actual structure of samarskite-(Y)? A TEM investigation of metamict samarskite from the Garnet Codera dike pegmatite (Central Italian Alps). American Mineralogist, 101, 1679–1690.

Černy, P. and Ercit, T.S. (1989) Mineralogy of niobium and tantalum: crystal chemical relationships, paragenetic aspects and their economic implications. In: Möller P, Černy P, Saupé F (eds) Lanthanides, tantalum and niobium. Springer, Berlin Heidelberg New York, pp 27–79.

Cliff, G. and Lorimer, G.W. (1975) The quantitative analysis of thin specimens. Journal of Microscopy, 103, 203–207.

Doyle, P.A. and Turner, P.S. (1968) Relativistic Hartree-Fock X-ray and electron Scattering factors. Acta Crystallographica section A, 24, 390–397.

Ewing, R.C. (1999) Nuclear waste forms for actinides. Proceedings of the National Academy of Sciences, 96, 60–73.

Gao, Y. and Elder, S.A. (2000) TEM study of TiO_2 nanocrystals with different particle size and shape. Materials Letters, 44, 228–232.

Hanson, S.L., Simmons, W.B., Webber, K.L., Falster, A.U. (1992) Rare-earth-element mineralogy of granitic pegmatites in the Trout Creek Pass district, Chaffee County, Colorado. Canadian Mineralogist, 30, 673–686.

Harley, S.L. and Kelly, N.M. (2007) Zircon, tiny but timely. Elements, 3, 13–18.

Hay, D.C. and Dempster, T.J. (2009) Zircon alteration, formation and preservation in sandstones. Sedimentology, 56, 2175–2191.

Hedenquist, J.W., Arribas, A., Eliseo, G.-U. (2000) Exploration for epithermal gold deposits. In S.G. Hagemann and P.E. Brown, Eds., Gold in 2000, 13, 245–277. Society of Economic Geologists Reviews, Littleton, Colorado.

Hirano, M. and Sato, S. (2011) Hydrothermal synthesis of yttrium and niobium co-doped anatase-type titania nanoparticles. Journal of the Ceramic Society of Japan, 119[6], 464–469.

Horn, M., Schwerdtfeger, C.F., Meagher, E.P. (1972) Refinement of the structure of anatase at several temperatures. Zeitschrift für Kristallograhie. 136, 273–281.

Hoskin, P.W.O. and Schaltegger, U. (2003) The composition of zircon in igneous and metamorphic petrogenesis. In: Hanchar, J.M., Hoskin, P.W.O. (eds) Zircon. Mineralogical Society of America Reviews in Mineralogy & Geochemistry, 53, 27–62.

Levchenko, A.A., Li, G., Boerio-Goates, J., Woodfield, B.F., Navrotsky, A. (2006) TiO_2 stability landscape: polymorphism, surface energy, and bound water energetics. Chemistry of Materials, 18, 6324–6332.

Macdonald, R., Bagiński, B., Kartashov, P., Zozulya, D. Dzierżanowski, P. (2015) Hydrothermal alteration of chevkinite-group minerals. Part 2. Metasomatite from the Keivy massif, Kola Peninsula, Russia. Mineralogical Magazine, 79, 1039–1059.

Papoulis, D., Tsolis-Katagas , P., Kalampounias, A.G., Tsikouras, B. (2009) Progressive formation of halloysite from the hydrothermal alteration of biotite and the formation mechanisms of anatase in altered volcanic rocks from Limnos Island, northeast Aegean Sea, Greece. Clays and Clay Minerals, 57, 566–577.

Papoutsa, A.D. and Pe-Piper, G. (2013) The relationship between REE-Y-Nb-Th minerals and the evolution of an A-type granite, Wentworth Pluton, Nova Scotia. American Mineralogist, 98, 444–462.

Penn, R.L. and Banfield, J.F. (1999) Morphology development and crystal growth in nanocrystalline aggregates under hydrothermal conditions: Insights from titania. Geochimica et Cosmochimica Acta, 63, 1549–1557.

Pezzotta, F., Diella, V., Guastoni, A. (1999) Chemical and paragenetic data on gadolinite-group minerals from Baveno and Cuasso al Monte, southern Alps, Italy. American Mineralogist, 84, 782–789.

Pezzotta, F., Diella, V., Guastoni, A. (2005) Scandium silicates from the Baveno and Cuasso al Monte NYF-granites, Southern Alps (Italy): Mineralogy and genetic inferences. American Mineralogist, 90, 1442–1452.

Pinarelli, L., Boriani, A., Del Moro, A. (1993) The Pb isotopic systematics during crustal contamination of subcrustal magmas: The Hercynian magmatism in the Serie dei Laghi (Southern Alps, Italy). Lithos, 31, 51–61.

Pinarelli, L., Del Moro, A., Boriani, A., Caironi, V. (2002) Sr, Ni, isotope evidence for an enriched mantle component in the origins of the Hercynian gabbro-granite series of the "Serie dei Laghi" (Southern Alps, NW Italy). European Journal of Mineralogy, 14, 403–415.

Post, J.E. and Burnham, C.W. (1986) Ionic modeling of mineral structures and energies in the electron gas approximation: TiO_2 polymorphs, quartz, forsterite, diopside. American Mineralogist, 71, 142–150.

Prol-Ledesma, R.M., Melgarejo, J.C., Martin, R.F. (2012) The El Muerto “NYF” granitic pegmatite, Oaxaca, Mexico, and its striking enrichment in allanite-(Ce) and monazite-(Ce). The Canadian Mineralogist, 50, 1055–1076.

Rapp, J.F., Klemme, S., Butler, I.B., Harley, S.L. (2010) Extremely high solubility of rutile in chloride and fluoride-bearing metamorphic fluids: An experimental investigation. Geology, 38, 323–326.

Rasmussen, B. (2005) Zircon growth in very low grade metasedimentary rocks: evidence for zirconium mobility at 250 °C. Contribution to Mineralogy and Petrology, 150, 146–155.

Robinson, K., Gibbs, G.V., Ribbe, P.H., (1971) The structure of zircon: A comparison with garnet. American Mineralogist, 56, 782–790.

Sabyrov, K., Burrows, N.D., and Penn, R.L. (2013) Size-dependent anatase to rutile phase transformation and particle growth. Chemistry of Materials, 25, 1408–1415.

Schaltegger, U. (2007) Hydrothermal zircon, Elements, 3(1), 51.

Shannon, R. D. (1976) Revised effective ionic radii and systematic studies of interatomic distances in halides and chalcogenides. Acta Crystallographica, A32, 751–767.

Sheldrick, G.M. (1997) SHELXL97: program for the refinement of crystal structures. University of Gottingen, Gottingen.

Smith, S.J., Stevens, R., Liu, S., Li, G., Navrotsky, A., Boerio-Goates, J., Woodfield, B.F. (2009) Heat capacities and thermodynamic functions of TiO_2 anatase and rutile: Analysis of phase stability. American Mineralogist, 94, 236–243.

Tanis, E.A., Simon, A., Tschauner, O., Chow, P., Xiao, Y., Burnley, P., Cline, C.J. II, Hanchar, J.M., Pettke, T., Shen, G., Zhao, Y. (2015) The mobility of Nb in rutile-saturated NaCl- and NaF-bearing aqueous fluids from 1–6.5 GPa and 300–800 °C. American Mineralogist, 100, 1600–1609.

Timofeev, A., Migdisov, A.A., Williams-Jones, A.E. (2015) An experimental study of the solubility and speciation of niobium in fluoride-bearing aqueous solutions at elevated temperature. Geochimica et Cosmochimica Acta, 158, 103–111.

Wirth, R. (2009) Focused Ion Beam (FIB) combined with SEM and TEM: Advanced analytical tools for studies of chemical composition, microstructure and crystal structure in geomaterials on a nanometre scale. Chemical Geology, 261, 217–229.

Zaban, A., Aruna, S.T., Tirosh, S., Gregg, B.A., Mastai, Y.J. (2000) The Effect of the Preparation Condition of TiO_2 Colloids on Their Surface Structures. Journal of Physical Chemistry B, 104, 4130–4133.

Zhang, H. and Banfield, J.F. (1998) Thermodynamic analysis of phase stability of nanocrystalline titania. Journal of Materials Chemistry, 8, 2073–2076.

Caption to Figures and Tables

Figure 1. (a) TiO_6 polyhedra arrangement in the anatase structure (Horn et al. 1972) as seen down [100] (*c* vertical); (b) SiO_4 and ZrO_8 polyhedra arrangement in the structure of zircon (Robinson et al. 1971) as seen down [100] (*c* vertical); (c) A-site cations (gray circles) and B-site octahedra (red) arrangement in the structure of aeschynite (this study) as seen down [010] (*c* vertical). These three structures are unrelated to each other, i.e., do not share any common feature(s) such as oxygen packing or polyhedral arrangement, consistently with the lack of crystallographic orientational relationship.

Figure 2. Map of the Hercynian plutonic and volcanic rocks in the Southern Alps and the locality of Cuasso al Monte (From Pezzotta et al. 2005, modified).

Figure 3. Optical stereomicrograph of a millimeter sized geode within the granophyre from Cuasso al Monte. a) The large orange crystals forming most of the mineral association are K-feldspar; lamellar

translucent crystals as in the lower left are albite (which also forms overgrowths on K-feldspar); the translucent mineral with botryoidal appearance at the center is fluorite and the translucent, faceted grain above fluorite is quartz; dark crystals are chamosite and anatase in granular aggregates. Chamosite forms lamellar, black-greenish grains (b) with iridescence due to zircon-coated anatase (not resolved). The small, orange, discoidal crystals with earthy luster at the center of the image are REE-carbonates (photograph width ~5 (a) and 1 mm (b)).

Figure 4. SEM-BSE images (a to c) and TEM-BF image (d) of anatase, zircon, and aeschynite: a) anatase truncated tetragonal bipyramids. Note the roughness of the surface and the etch marks on pinacoidal and pyramidal facets; b) arborescent crystals of aeschynite on anatase; c) high magnification image of the anatase surface: the roughness is due to submicroscopic lenticular crystals in random orientation; d) a cross section across the zircon-anatase interface. Note the strained interface separating the randomly oriented zircon (Zrn) crystals from anatase (Ant). Some dislocations in anatase are also indicated (arrows).

Figure 5. Compositional profile across the anatase/zircon interface for a distance of about 600 nm. The shadowed region in the plot corresponds to the band showing strain contrast and outlined by dashed lines in the inset. The inset also shows the trace of the compositional profile as resulting from the contamination stains formed at beam positions during spot analysis collection, which were taken at intervals of ~50 nm (crosses). Note the Nb maximum at the anatase/zircon interface.

Figure 6. a) BF-TEM image of an arborescent crystal picked up from the miarolitic cavity and put on a carbon coated Cu-grid and (b) related SAED taken with the incident beam parallel to [001]. This

pattern is consistent, within the experimental error and net of dynamical effects – 0*k*l for $k = 2n$ only – with aeschynite (*Pnma*, a ~10.80, b ~7.68, c ~5.10 Å, Capitani et al. 2016). c) HR-TEM image showing mottled contrast typical of metamict minerals, with brighter areas lacking of long-range order (arrows). The main lattice planes within a crystalline area (square) are showed (inset). d) Representative EDS spectrum (Cu peaks are from the grid).

Table 1. Semi-quantitative TEM-EDS compositions of anatase and zircon (average of 6 and 8 spot analyses, respectively) calculated on the basis of 4 oxygens (one sigma relative error in brackets; values in italics when below the 2 sigma level).

Table 2. Experimental EDT data collection parameters and crystallographic information for aeschynite.

Table 3. TEM-EDS compositions of niobioaeschynite crystals calculated on the basis of tree cations per formula unit (one sigma relative error in brackets) and their average (standard deviation in brackets). Ca, Fe, Y, Pb, Th and U are assigned to the A-site; Al, Ti, As, and Nb to the B-site.

This is a preprint, the final version is subject to change, of the American Mineralogist (MSA)
Cite as Authors (Year) Title. American Mineralogist, in press.
DOI: http://dx.doi.org/10.2138/am-2018-6242

Fig. 1 a b c

This is a preprint, the final version is subject to change, of the American Mineralogist (MSA)
Cite as Authors (Year) Title. American Mineralogist, in press.
DOI: http://dx.doi.org/10.2138/am-2018-6242

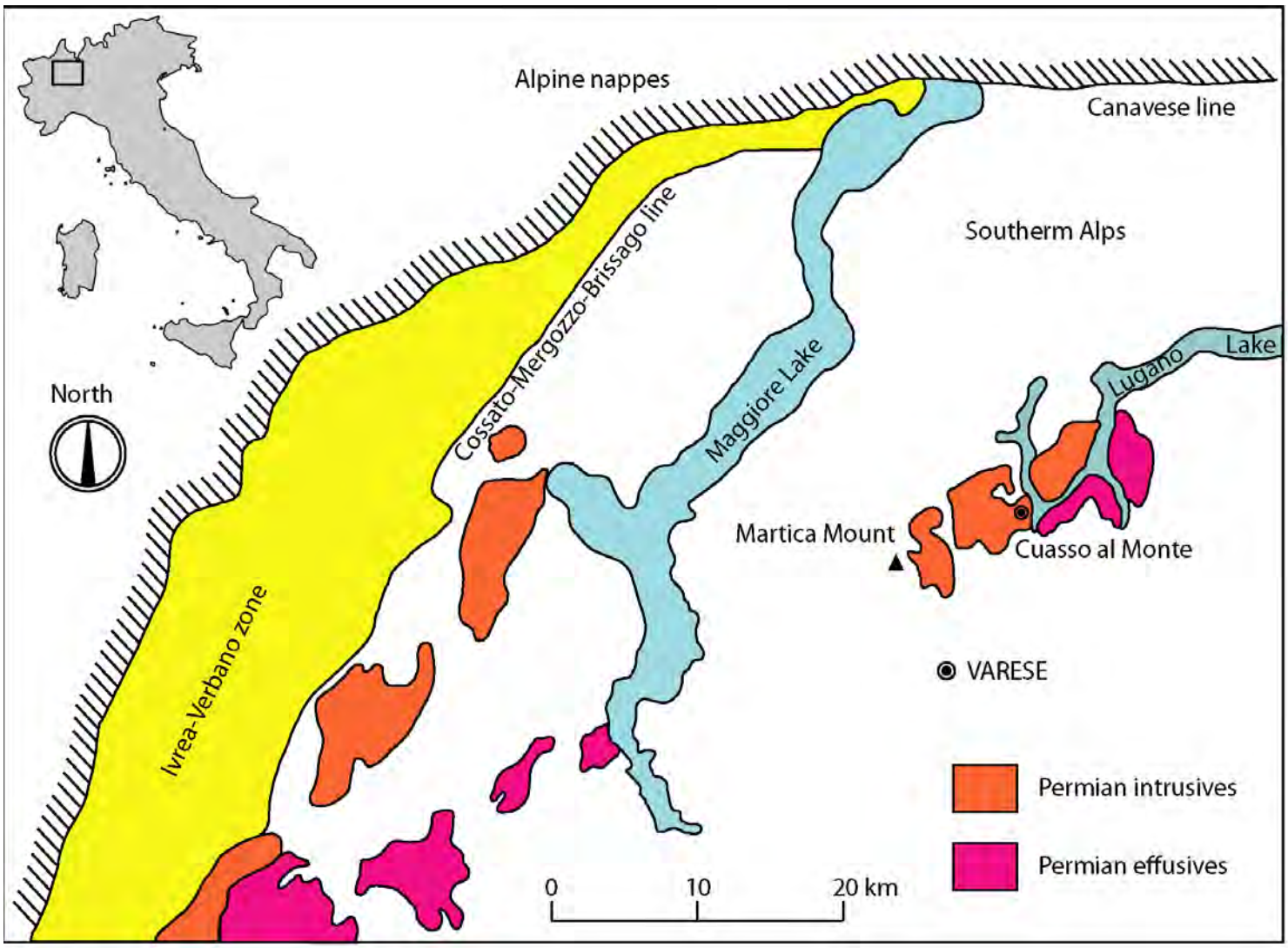

Fig.2

This is a preprint, the final version is subject to change, of the American Mineralogist (MSA)
Cite as Authors (Year) Title. American Mineralogist, in press.
DOI: http://dx.doi.org/10.2138/am-2018-6242

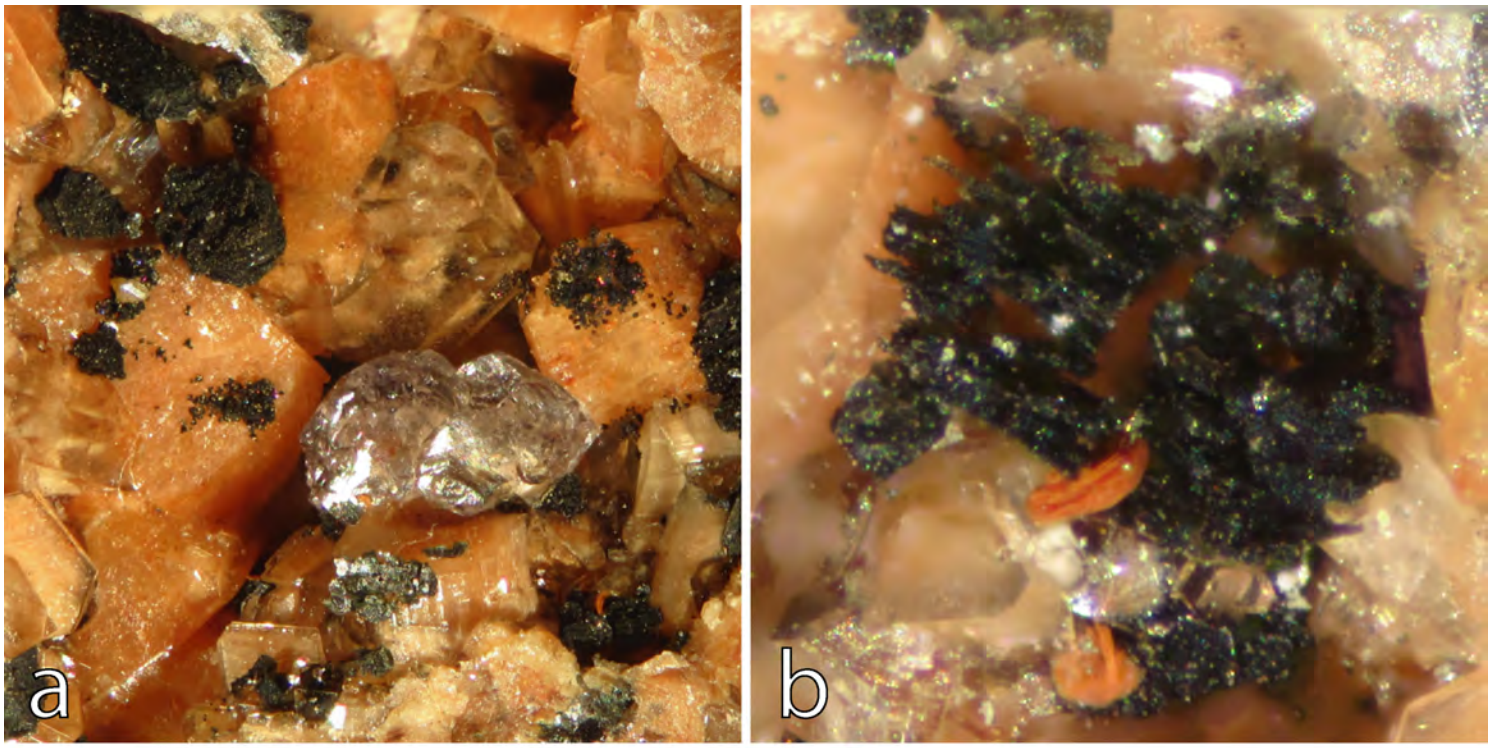

Fig. 3

This is a preprint, the final version is subject to change, of the American Mineralogist (MSA)
Cite as Authors (Year) Title. American Mineralogist, in press.
DOI: http://dx.doi.org/10.2138/am-2018-6242

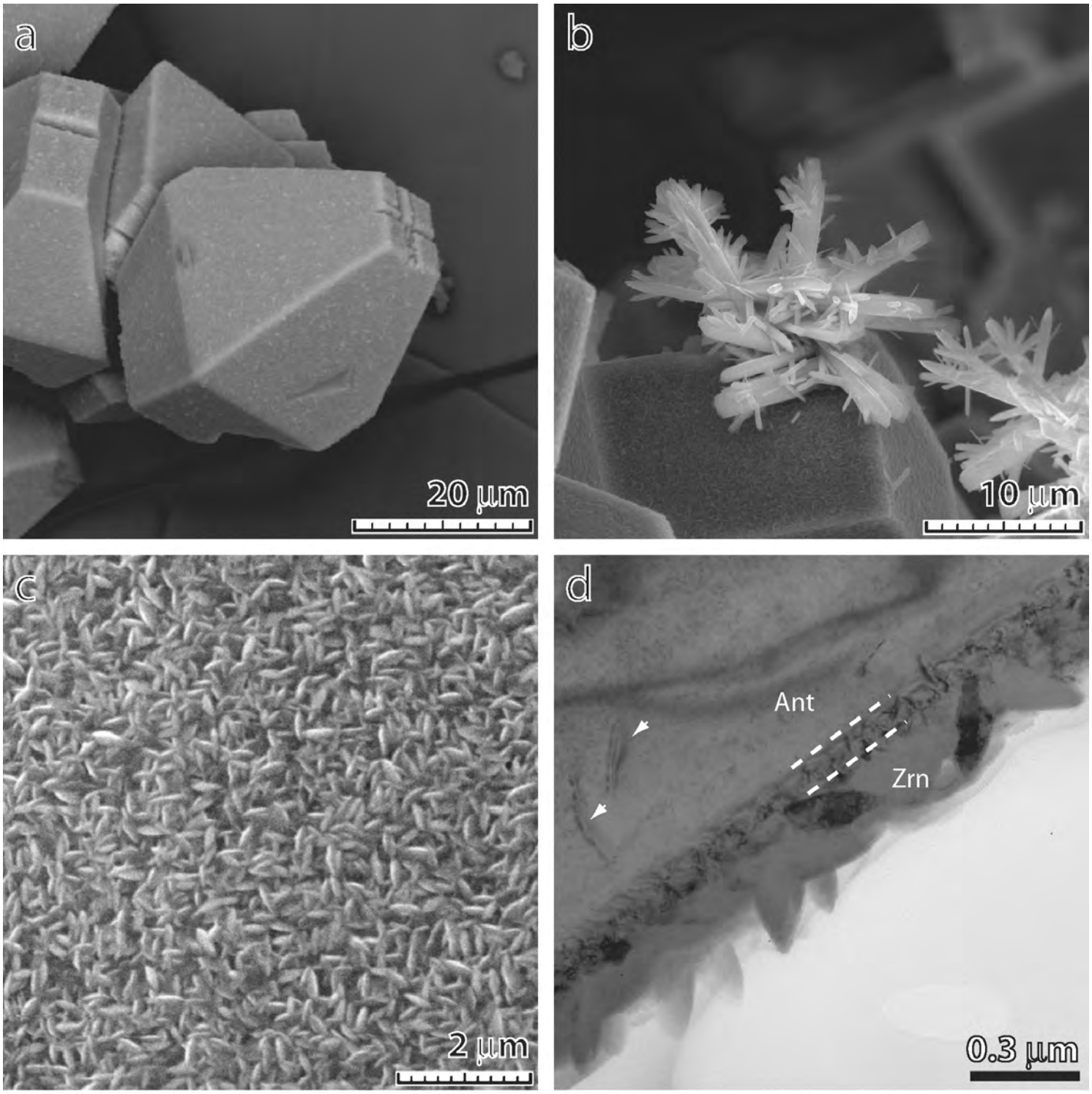

Fig. 4

This is a preprint, the final version is subject to change, of the American Mineralogist (MSA)
Cite as Authors (Year) Title. American Mineralogist, in press.
DOI: http://dx.doi.org/10.2138/am-2018-6242

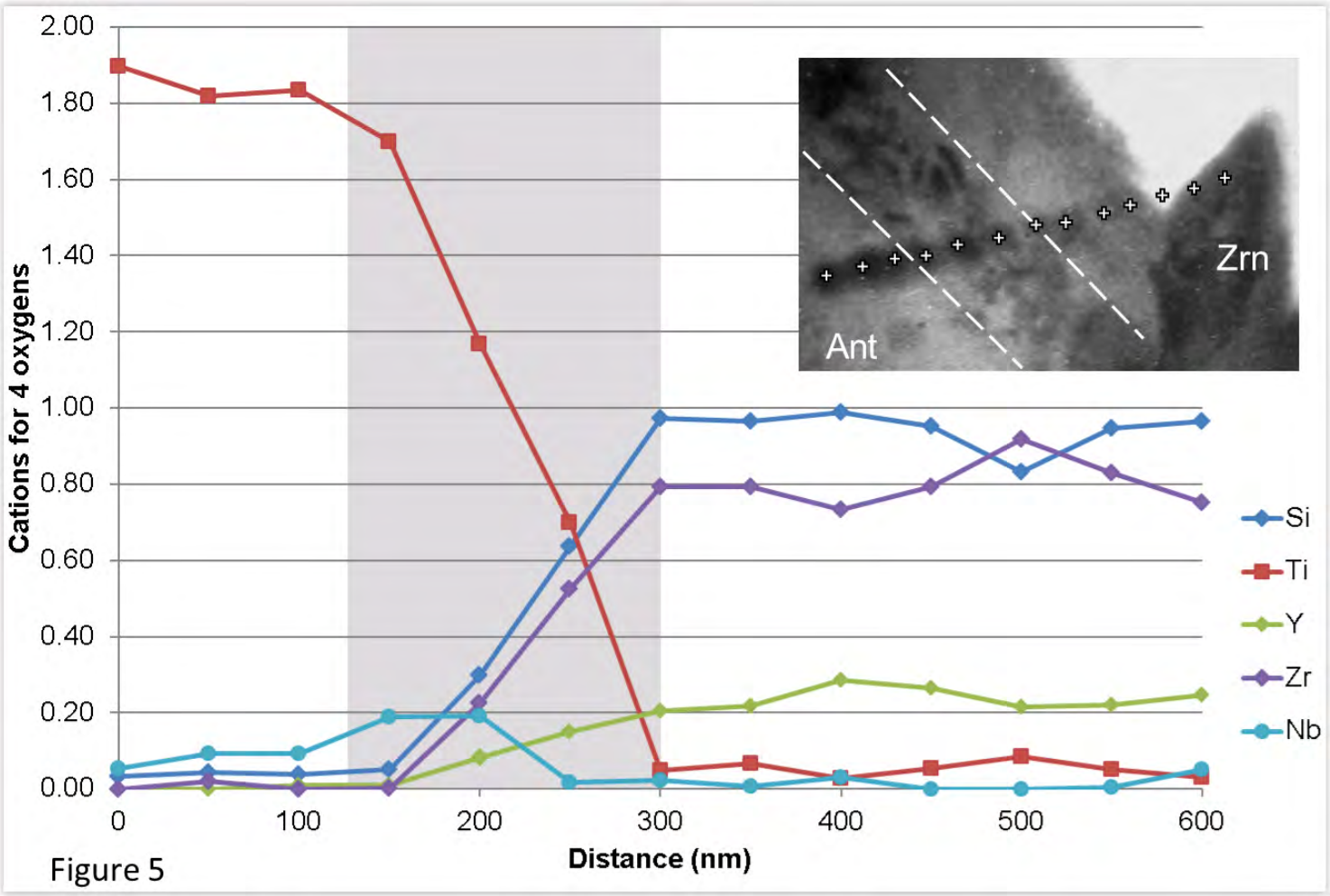

Figure 5

This is a preprint, the final version is subject to change, of the American Mineralogist (MSA)
Cite as Authors (Year) Title. American Mineralogist, in press.
DOI: http://dx.doi.org/10.2138/am-2018-6242

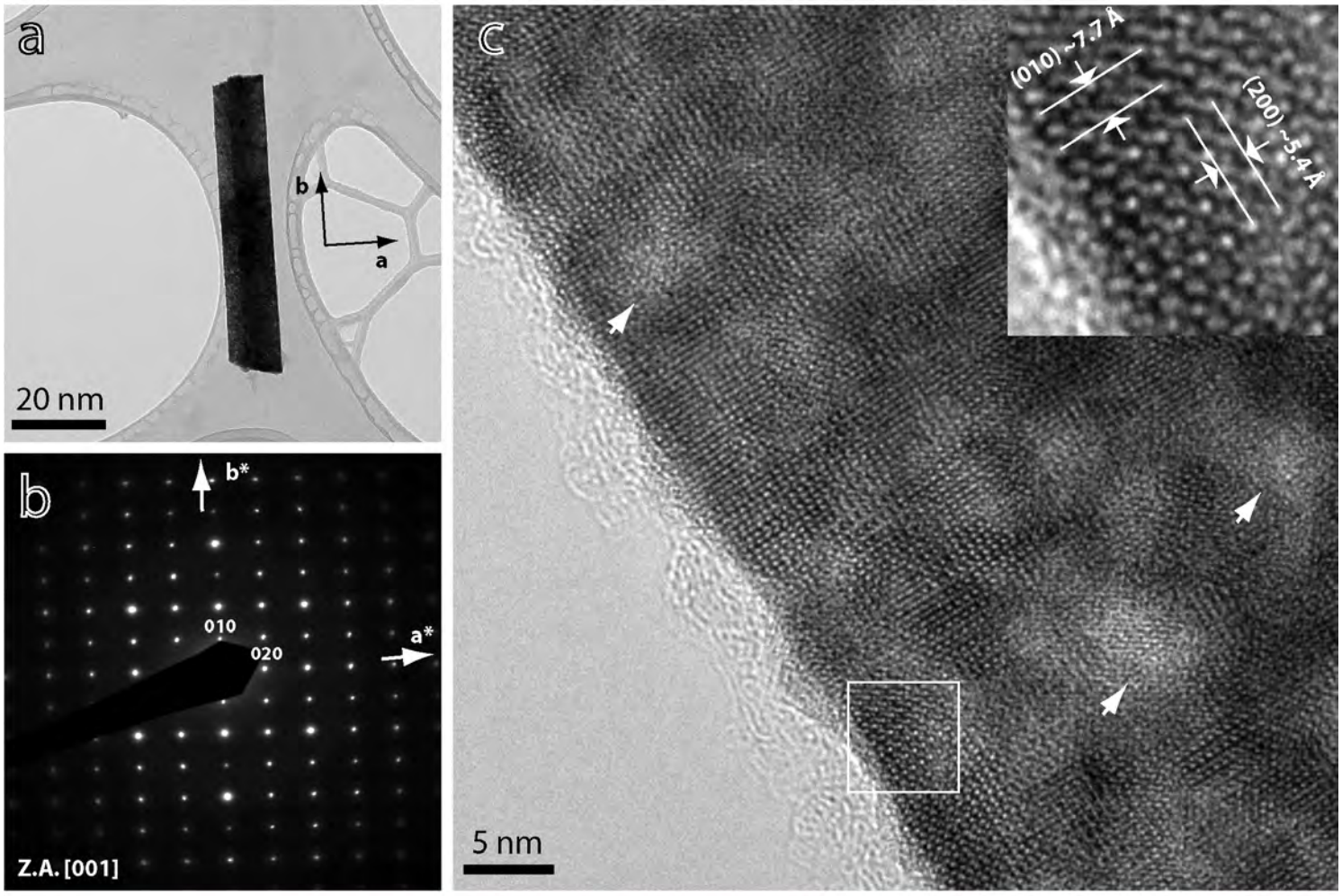

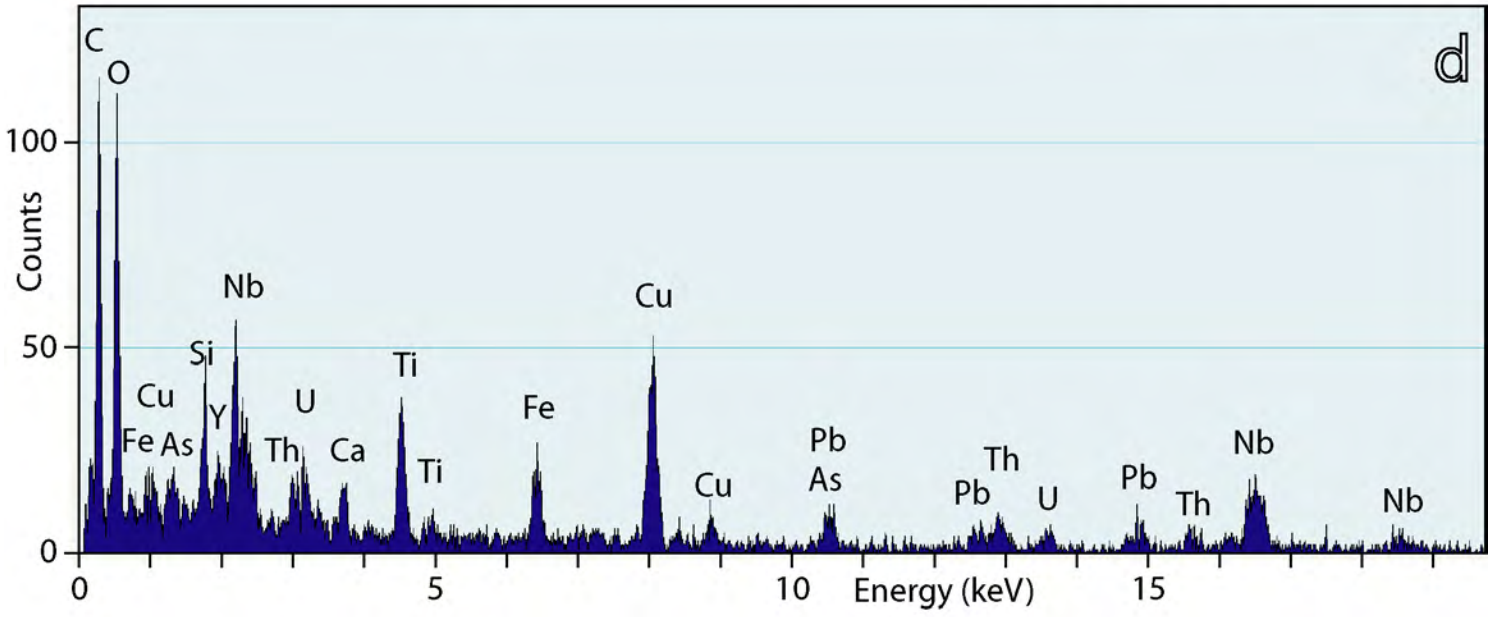

Fig. 6

This is a preprint, the final version is subject to change, of the American Mineralogist (MSA)
Cite as Authors (Year) Title. American Mineralogist, in press.
DOI: http://dx.doi.org/10.2138/am-2018-6242

Table 1. Semi-quantitative TEM-EDS compositions of anatase and zircon (average of 6 and 8 spot analyses, respectively) calculated on the basis of 4 oxygens (one sigma relative error in brackets; values in italics when below the 2 sigma level).

	Anatase		Zircon	
	Mean	Range	Mean	Range
Si	0.03(1)	0.01 - 0.04	0.97(8)	0.91 - 0.99
Ti	1.89(4)	1.83 - 1.94	0.05(1)	0.03 - 0.07
Y	*0.00(1)*	*0.00 - 0.01*	0.25(6)	0.21 - 0.32
Zr	*0.00(2)*	*0.00 - 0.02*	0.78(6)	0.73 - 0.83
Nb	0.06(2)	0.03 - 0.09	*0.02(5)*	*0.00 - 0.05*
Cat	1.99	1.98 - 2.00	2.06	2.05 - 2.11

This is a preprint, the final version is subject to change, of the American Mineralogist (MSA)
Cite as Authors (Year) Title. American Mineralogist, in press.
DOI: http://dx.doi.org/10.2138/am-2018-6242

Table 2. Experimental EDT data collection parameters and crystallographic information for aeschynite.

System	(Fe,Ca,Th,U,Y,Pb)(Nb,Ti,Al, As)$_2$O$_6$
Tilt range α(°); β(°)	–30/+26; –29/+30
Tilt step (°)/precession angle (°)	1/1
Crystal size (μ)	~1.39 × 0.23 × 0.02
a, b, c (Å)	11.21(1), 7.73(1), 5.24(1)
Space Group	*Pnma*
Total/ independent reflections	1580/400
Resolution (Å)/coverage(%)	0.80/79.4
Limiting indices	$-13 \le h \le 13, -9 \le k \le 9, -5 \le l \le 5$
$R_{(int)}$	0.3230
R_1/all	0.3047/400
R_{4s}/refl. with $F_o > 4\sigma(F_o)$	0.2537/316

This is a preprint, the final version is subject to change, of the American Mineralogist (MSA)
Cite as Authors (Year) Title. American Mineralogist, in press.
DOI: http://dx.doi.org/10.2138/am-2018-6242

Table 3. TEM-EDS compositions of niobioaeschynite crystals calculated on the basis of tree cations per formula unit (one sigma relative error in brackets) and their average (standard deviation in brackets). Ca, Fe, Y, Pb, Th and U are assigned to the A-site; Al, Ti, As, and Nb to the B-site.

	xx 1		xx 2		xx 3		Mean
	1	2	3	4	5	6	
Al	0.08(3)	0.15(1)	0.16(2)	0.18(2)	0.17(4)	0.08(4)	0.14(5)
Ca	0.16(4)	0.25(1)	0.20(2)	0.23(2)	0.28(3)	0.20(3)	0.22(4)
Ti	0.58(5)	0.72(2)	0.82(3)	0.63(3)	0.59(4)	0.77(5)	0.69(10)
Fe^{2+}	0.30(4)	0.35(2)	0.32(2)	0.30(2)	0.46(4)	0.39(4)	0.35(6)
As^{3+}	0.05(6)	0.00 -	0.07(3)	0.00 -	0.11(3)	0.12(3)	0.06(5)
Y	0.07(4)	0.17(2)	0.10(2)	0.09(2)	0.05(5)	0.10(5)	0.10(4)
Nb	1.31(10)	1.04(4)	0.98(5)	1.22(6)	0.93(6)	0.83(6)	1.05(18)
Pb^{2+}	0.12(6)	0.11(2)	0.07(2)	0.07(1)	0.15(2)	0.15(3)	0.11(3)
Th	0.25(4)	0.15(1)	0.14(2)	0.14(2)	0.12(2)	0.12(2)	0.15(5)
U^{4+}	0.08(4)	0.05(1)	0.14(2)	0.13(2)	0.13(2)	0.25(3)	0.13(7)
$\sum_A$	0.98	1.08	0.97	0.97	1.19	1.20	1.06
$\sum_B$	2.02	1.92	2.03	2.03	1.81	1.80	1.94

Notes: Analyses on xx1 and xx1 were acquired with the Edax EDS system; analyses on xx3 with the Oxford EDS system. The latter refers to the crystal studied by P-EDT.